The NMR Phased Array

P. B. ROEMER,* W. A. EDELSTEIN,* C. E. HAYES,† S. P. SOUZA,*
AND O. M. MUELLER*

*GE Corporate Research and Development Center, Schenectady, New York 12301;
†GE Medical Systems, Milwaukee, Wisconsin 53201

We describe methods for simultaneously acquiring and subsequently combining data from
a multitude of closely positioned NMR receiving coils. The approach is conceptually similar
to phased array radar and ultrasound and hence we call our techniques the "NMR phased
array." The NMR phased array offers the signal-to-noise ratio (SNR) and resolution of a
small surface coil over fields-of-view (FOV) normally associated with body imaging with no
increase in imaging time. The NMR phased array can be applied to both imaging and
spectroscopy for all pulse sequences. The problematic interactions among nearby surface
coils is eliminated (a) by overlapping adjacent coils to give zero mutual inductance, hence
zero interaction, and (b) by attaching low input impedance preamplifiers to all coils, thus
eliminating interference among next nearest and more distant neighbors. We derive an al-
gorithm for combining the data from the phased array elements to yield an image with
optimum SNR. Other techniques which are easier to implement at the cost of lower SNR
are explored. Phased array imaging is demonstrated with high resolution (512 × 512, 48-
cm FOV, and 32-cm FOV) spin-echo images of the thoracic and lumbar spine. Data were
acquired from four-element linear spine arrays, the first made of 12-cm square coils and the
second made of 8-cm square coils. When compared with images from a single 15 × 30-cm
rectangular coil and identical imaging parameters, the phased array yields a 2 × and 3 × higher
SNR at the depth of the spine (~7 cm). © 1990 Academic Press, Inc.

INTRODUCTION

We describe here a method of *simultaneously* receiving NMR signals from a mul-
titude of overlapping and closely positioned RF coils which can cover 100% of a region
of interest (*1, 2*). Two important examples of coil arrays are (1) a linear and (2) a
two-dimensional array of small surface coils applied to the plane, or nearly plane,
surface of a sample volume. Another example is an array of coils which surrounds a
sample volume. Each coil is associated with an independent preamplifier and receiver
chain. The outputs from the receiver chains are digitized, saved, and then phase shifted
and combined in an optimum manner dependent on the point in space from which
the signal originated. In this way, we obtain the high signal-to-noise ratio (SNR) of
surface coils along with a large field-of-view (FOV) usually associated with volume
imaging coils, and there is no imaging time penalty. We therefore approach the op-
timum performance of the NMR system.

By overlapping adjacent coils and connecting all coils to low input impedance
preamplifiers, we have eliminated problematic interactions between coils with over-

pping FOVs. We have developed a mathematical theory of the best way to construct
a single image from the data of many coils. We also evaluate the efficiencies of other,
less demanding algorithms. The same approaches can be used to produce optimized
spectra by combining spectroscopic data from multiple RF coils.

The simultaneous reception in an array of RF coils is analogous to the operation
of phased array used in radar or ultrasound. We therefore should not think of the
array as a collection of independent coils but consider it a single object we call the
"NMR phased array."

The NMR phased array has profound implications for data acquisition/processing
as it expands data handling requirements by factors from 10 to 100 or more.

OPTIMIZING SNR FOR A THREE-DIMENSIONAL VOLUME

A singular circular surface coil of diameter d gives the highest possible SNR for a
volume at depth d inside a conducting infinite half space (3, 4). However, a single
surface coil can only effectively image a limited region whose dimensions are com-
parable to the diameter of the surface coil. For a planar NMR phased array consisting
of circular coils of diameter d, it is evident that we optimize the SNR for a planar
region at depth $\sim d$ and thereby approach the ultimate SNR for that depth (4). In
fact, an NMR phased array of coils with characteristic dimension d wrapped around
a sample approaches the ultimate SNR from depth d to the center of the sample. This
is because the signals from many coils are combined with weights depending on the
position of the image voxel. For points at depths greater than d, a separate optimum
coil is synthesized for each point in the volume. For points at depths less than d the
optimum coil cannot be synthesized for each point and improvements in the SNR
can be obtained by making the coils smaller.

The NMR phased array has the additional property that the correct polarization of
signal reception (i.e., circular or elliptical) at each point is accomplished automatically.
This is done by the choice of phases and amplitudes for combining the instantaneous
NMR signals.

An estimate of an upper limit on the number of coils that one might consider for
a phased array can be made by recognizing that the maximum extent of the array is
limited by the magnet homogeneity which allows useful NMR to be done, a region
typically the size of a 50-cm sphere. If the coils are to be placed on a cylindrical form
with a 20-cm radius and 50-cm length, we would have 6000 cm^2 of surface area for
coils. Full coverage of this area with 8-cm coils would require about 100 coils. Perhaps
not all coils would be used all the time, but a substantial fraction might. Since each
coil requires its own receiver and data acquisition hardware, practical considerations
favor fewer coils.

SWITCHED VERSUS SIMULTANEOUS ARRAYS

The idea of receiving from a number of closely positioned surface coils has been
discussed in the literature (5-7). A true NMR phased array requires both full coverage
of the sample and simultaneous reception, and no practical methods for achieving
these goals with many coils have hitherto been described.

Numerous papers appear in the literature in which the outputs from a number of

surface coils are switched between excitations to avoid interactions (7–11). Since these coils are not concurrently active, only one coil can be associated with a particular slice. Thus switched coils offer SNR advantages over a single coil when slices are widely separated. Hardy *et al.* used this technique for bilateral imaging of the temporomandibular joint (8) and Boskamp showed results for multislice axial imaging of the body (10) with widely separated slices.

Large FOV sagittal slices as demonstrated in this paper are an example of imaging in which switched coils do not offer any FOV advantages over a single coil. Another example is 3D imaging. In 3D each excitation contributes in part to every voxel in the data set and thus switched coils do not add any advantage over a single coil. On the other hand, all coils in the NMR phased array receive data simultaneously from all regions of the sample, independent of the pulse sequence. Thus they receive all the information available over the sample volume at the best possible SNR for each point within the sample.

COIL INTERACTIONS AND THEIR ELIMINATION

Consider a pair of identical resonant loops that are tuned to the same resonant frequency f_0. If the loops are placed near each other, the mutual inductance between coils causes the resonances to split as indicated in Fig. 1. The splitting results in a loss of sensitivity at the frequency f_0. Signal and noise are also transferred from one coil to another through the mutual inductance. To eliminate or reduce this coupling we use two techniques. First, adjacent coils are overlapped to force the mutual inductance to zero as shown in Fig. 2. Second, all coils are connected to low input impedance preamplifiers to reduce coupling between coils that are not overlapped. This results in coils that behave independently although all coils are simultaneously active and receiving NMR signals.

The technique of overlapping to eliminate the mutual inductance of adjacent coils can be used to form a one-dimensional spine array as in Fig. 3 or a two-dimensional
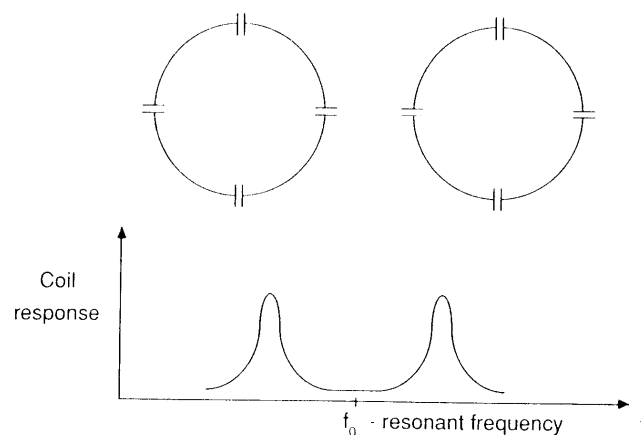

Coil
response

f_0 · resonant frequency   f

FIG. 1. Response of two adjacent surface coils tuned to the same frequency f_0. The original resonances split into two resonances and the sensitivity of the coils at frequency f_0 is greatly reduced.

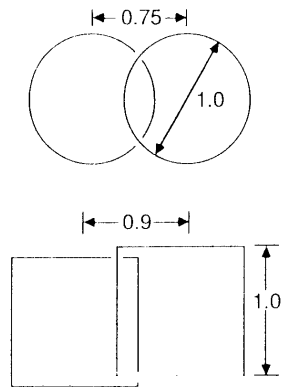|←— 0.75 —→|

1.0

|←— 0.9 —→|

1.0

FIG. 2. Immediately adjacent coils are overlapped to set their mutual inductance to zero eliminating the problem of splitting resonances for nearest neighbors. The centers of the circular loops are separated by about 0.75× their diameter, and square loops by about 0.9× diameter. The exact overlap depends on coil details and is determined empirically.

array as shown in Fig. 4. Remaining is a small but significant interaction between next nearest neighbors and farther coils. This interaction is reduced to negligible levels by connecting all coils to low input impedance preamplifiers. To understand how this reduces coupling, consider two interacting surface coils modeled as primary and secondary of a transformer (Fig. 5). First we examine how the components are chosen for impedance matching to the preamplifier. For coil 2 in isolation and at the resonant
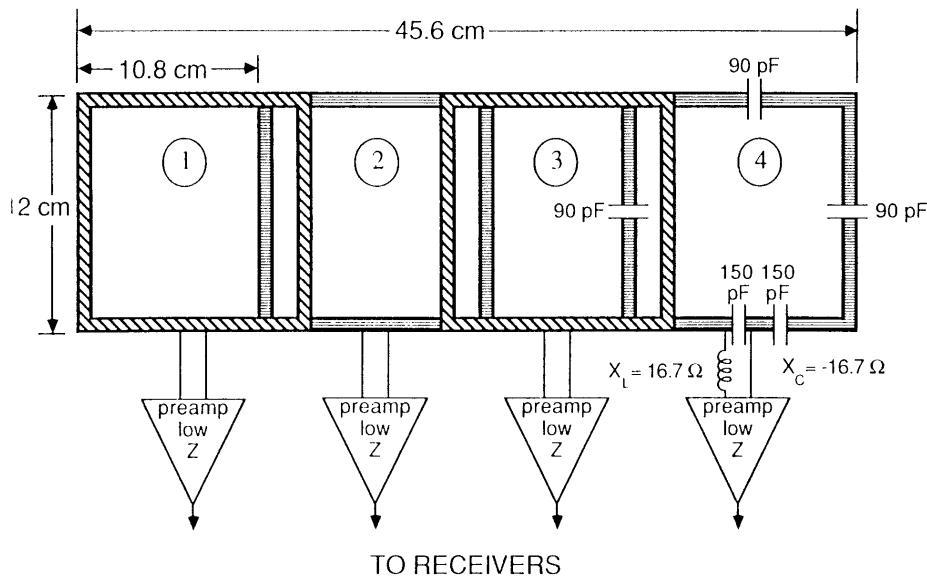

TO RECEIVERS

FIG. 3. Four element linear spine coil. Nearest neighbor interactions are eliminated by overlap. Next nearest neighbor and more distant coil interactions are reduced to negligible levels by connection to low input impedance preamplifiers.
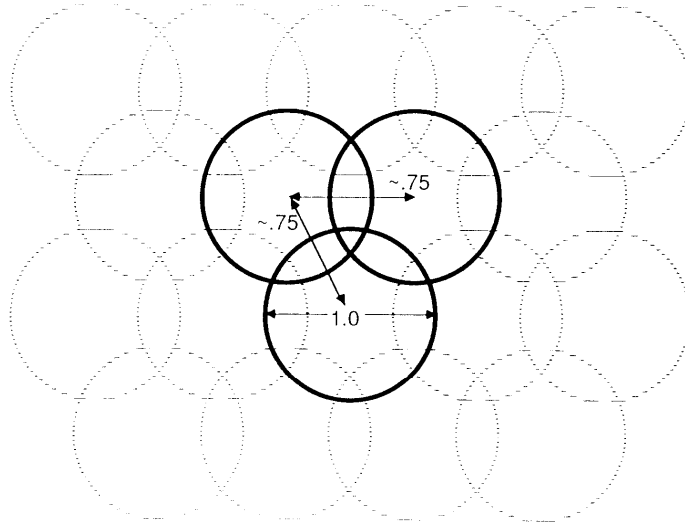
FIG. 4. 2D surface coil array. Nearest neighbor interactions are eliminated by overlap. Next nearest neighbor and more distant coil interactions are reduced to negligible levels by connection to low input impedance preamplifiers.

frequency we determine that the impedance of the coil as viewed at the preamplifier is

$$Z_b = \frac{X^2_{C_{2b}}}{R_1} + j(X_{L_{2b}} - X_{C_{2b}}). \qquad [1]$$

To transform the series resistance, R_1, to 50 Ω real the proper choice of $X_{C_{2b}}$ and $X_{L_{2b}}$ is

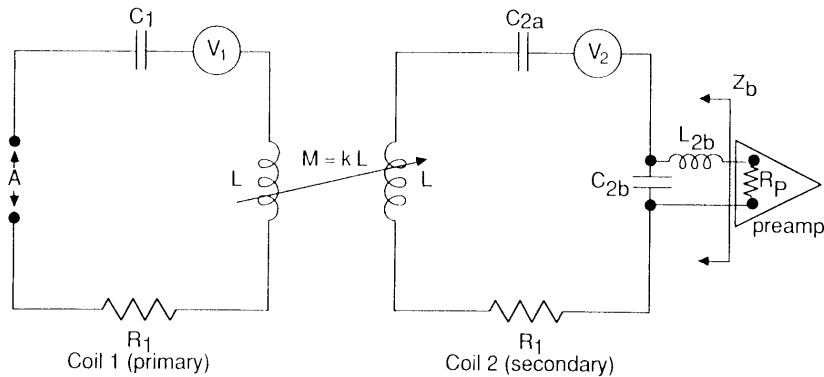$$X_{L_{2b}} = X_{C_{2b}} = \sqrt{50 R_1} \equiv X_2. \qquad [2]$$

FIG. 5. Interacting surface coils modeled as primary and secondary of a transformer. The second coil has a preamplifier with input resistance R_P connected to its output. V_1 and V_2 are the NMR voltages induced in the coils.

L_{i} is not absolutely necessary for matching since the impedance is usually dominated by the real part of Eq. [1]. In our case, however, this inductor forms an important element in our deactivation circuit. To see this, consider the circuit comprising the elements C_{2b} and L_{2b} and the preamplifier. If the input impedance of the preamplifier is truly zero, the inductor L_{2b} forms a parallel resonant circuit with the output capacitor C_{2b} and blocks current from flowing in the surface coil even though the coil is receiving and faithfully transferring an NMR signal to the preamplifier. If very little current flows in the surface coil during reception, no noise or NMR signal is coupled to other coils and all coils receive independently.

The effectiveness of this method depends on values of impedances one can practically achieve. The lower the input impedance of the preamplifier, the greater the decoupling. The part of the preamplifier input circuit that gives the low input impedance (12) is shown in Fig. 6. The Gallium Arsenide MOSFET adds minimum noise if its noise source impedance is on the order of 1–2 kΩ. Therefore the input transformer, composed of the series inductor and capacitor, is chosen to be series resonant at the frequency of interest and is chosen to transform 50 Ω at the preamplifier input to 1250 Ω at the transistor. Since the transistor itself has a very high input impedance, the input impedance of the preamplifier is determined primarily by the series resonance circuit, which ideally is a short circuit at the resonant frequency. Using these techniques Mueller and Edelstein (12) have designed preamplifiers with very low input impedances (<3 Ω) and low noise figures (<0.5 db). Attaching the preamplifier to a $\lambda/2$ cable adds another 1–2 Ω. Thus we find a practical value for R_{P} in Fig. 5 to be about 5 Ω.

The coupling of noise and signal between two coils with low input impedance preamplifiers attached is very small. Suppose that both coils in Fig. 5 are independently tuned to the same resonant frequency ($X_{I} = X_{C_{2a}} = X_{C_{2b}} = 0$ and $X_{I} = X_{C_{1}} = 0$). Without the second coil present, the series impedance of the primary loop as viewed at terminal A is given by R_{1}. With the second coil present and connected to a preamplifier of input impedance R_{P} the impedance as viewed from the terminals of the primary is then given by

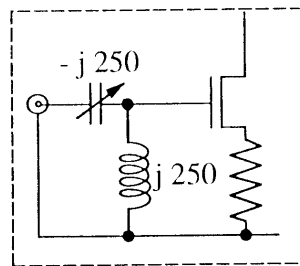$$Z_{A} = R_{1} + \frac{\omega^{2} L^{2} k^{2}}{R_{1} + (X_{2}^{2}/R_{P})}.$$
[3]

FIG. 6. Input circuit of preamplifier. The capacitor and resistor form a series resonant circuit that transforms 50 Ω at the input of the preamplifier to 1250 Ω at the input of the transistor. The high input impedance of the transistor allows the C and L of the preamplifier input transformer circuit to resonant. The preamplifier input impedance as viewed from its terminals is therefore very low (<3 Ω).

The second term of [3] represents the noise power coupled between coils. We see that if either the mutual inductance coupling constant k is made zero or the input impedance of the preamplifier is made zero, this term approaches zero and the resultant noise resistance is R_1, that of a single isolated coil.

In a similar manner we can now ask how much NMR signal is transferred between coils by determining the open circuit voltage as viewed at terminal A. The result is

$$V_A = V_1 - V_2 \frac{j\omega Lk}{R_1 + (X_2^2/R_P)}.\qquad [4]$$

Again we see that if either the mutual inductance or the preamplifier input impedance is zero, we obtain the NMR signal of the isolated coil.

Recognizing that the preamplifier and attached cable has a small ($<5\ \Omega$) but nonzero input impedance, we can estimate how much signal and noise is transferred between coils for the more practical case of the spine array of Fig. 3. The coil's series resistance, R_1, is about $0.5\ \Omega$ in air and about $5.5\ \Omega$ when placed on the back. For these conditions Table 1 shows results for the signal and noise transferred between coil 1 and 3. For comparison we include results for preamplifier input impedances of $50\ \Omega$ and ∞.

Under unloaded conditions Table 1 shows that with a low input impedance preamplifier ($R_P = 5\ \Omega$) attached to coil 3, the presence of coil 3 results in only a 2.4% increase in noise power as seen from the terminals of coil 1. If, on the other hand, a $50\ \Omega$ preamplifier is attached to coil 3, a 22% increase in the noise power occurs. Under loaded conditions the preamplifier input impedance is not particularly important. However, all coils in an array may not be heavily loaded and thus low input impedance preamplifiers are important.

Table 1 also indicates the limitation of using preamplifiers to decouple coils and the importance of overlapping adjacent coils. For example, suppose we have a coupling coefficient of 0.1, as might be the case for two coils relatively close to each other but not overlapped (see Fig. 9). The coupling of noise power is then $(0.1/0.007)^2$ or 204 times greater than the values given in Table 1. Even under the most forgiving circumstances, with $R_P = 5\ \Omega$ and a loaded coil, a 41% increase in noise power occurs. Thus we conclude the practical limits on the preamplifier input impedance combined with

TABLE 1

Noise Power and NMR Voltage Transfer between Coil 1 and Coil 3
of the Spine Array in Fig. 3

Condition	R_1 (Ω)	R_P (Ω)	Z_A/R_1	V_A
Unloaded	0.5	5.0	1.024	$V_1 - 0.015jV_2$
Unloaded	0.5	50	1.22	$V_1 - 0.135jV_2$
Unloaded	0.5	∞	3.65	$V_1 - 1.630jV_2$
Loaded	5.5	5.0	1.002	$V_1 - 0.013jV_2$
Loaded	5.5	50	1.011	$V_1 - 0.074jV_2$
Loaded	5.5	∞	1.022	$V_1 - 0.148jV_2$

Note. Equations [3] and [4] were used to calculate the table entries with the coupling coefficient $k = 0.007$, the Larmor frequency $f_0 = 64$ MHz, and $X_L = 116\ \Omega$.

the cable losses limit their use to decoupling of relatively weakly interacting coils. Adjacent coils still need to be overlapped.

IMAGE RECONSTRUCTION

Decoupling the surface coils allows data to be separately and simultaneously acquired from a multitude of coils. The resultant images/spectra are by themselves useful but the real utility becomes evident when the data is combined to form a single composite image in an automatic way. We present here a variety of methods for combining data based on SNR considerations. Using RF field maps, we derive the optimum way to combine complex quadrature data and the optimum way to combine magnitude data. We also show how to make a uniform sensitivity image and a uniform noise image from the combined data. Finally, we consider a sum-of-squares method which has the advantage that detailed RF field maps of the coil do not have to be known. The data combining methods are pulse sequence independent and apply to both imaging and spectroscopy.

Maximized SNR image. To understand how to obtain maximum SNR, we consider combining the signals through a series of lossless phase shifters and transformers as shown in Fig. 7. For coil i, the NMR voltage at the coil output is proportional to (*13*, *14*)

$$V_i(t) = \omega M V B_{ti} \cos(\omega t - \theta_i + \psi).$$ [5]

where V is the voxel volume, M is the magnetization density, B_{ti} is the magnitude of the transverse magnetic field for unit current in the coil, ψ is an arbitrary phase of the rotating nuclei, and θ_i is the angle of the RF magnetic field measured from some fixed reference in the laboratory frame. Increasing values of θ_i are in the direction of rotation of the precessing nuclei.

The total voltage at the output of the transformer is obtained by phase shifting and summing the outputs of the individual coils:
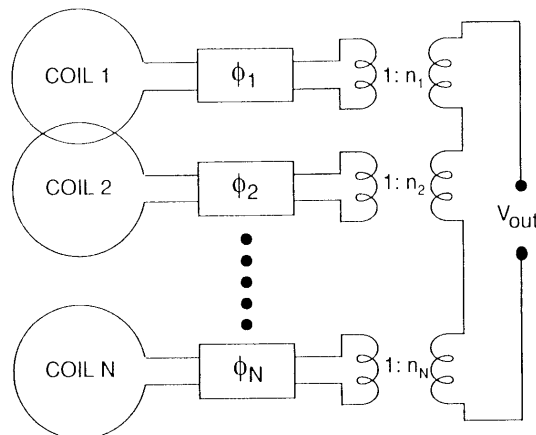
FIG. 7. Set of N coils with outputs phase shifted and summed through a set of lossless transformers.

$$V_{\text{tot}}(t) = \omega M V \sum_{i=1}^{N} n_i B_{ti} \cos(\omega t - \theta_i + \psi + \phi_i).$$ [6]

The signal-to-noise ratio at the output of the transformer is then defined as the ratio of the instantaneous NMR signal to the rms noise voltage

$$\text{SNR} \equiv \frac{|V_{\text{tot}}|}{\sqrt{4kT\Delta f R_{\text{tot}}}}.$$ [7]

where $|V_{\text{tot}}|$ is the magnitude of the voltage, R_{tot} is the total noise resistance as viewed from the output terminals, and Δf is the receiver bandwidth.

Since we have assumed that the phase shifters and transformer are lossless, [7] represents the intrinsic SNR (14) whereby the noise is caused by thermal fluctuations in the sample only. In this case, the noise resistance can be determined from the time-averaged, volume-integrated losses in the sample for a sinusoidal current of unit amplitude in the secondary of the transformer. If $E_i(x, y, z)$ is the spatial dependence of the electric field induced in the sample for a sinusoidal current of unit amplitude in coil i, the total noise resistance as seen at the output terminals is then

$$R_{\text{tot}} = \sum_{i=1}^{N} \sum_{k=1}^{N} n_i n_k R_{ik} \cos(\phi_i - \phi_k).$$ [8]

where n_i is the turns ratio of the transformers, ϕ_i is the phase shift applied to each signal before summing through the transformers, and R_{ik} is defined as the volume integral

$$R_{ik} \equiv \sigma \int E_i(x, y, z) \cdot E_k(x, y, z) dV.$$ [9]

The noise resistance matrix contains all the information about correlated and un-correlated noise between coils. R_{ii} is the noise resistance of coil i in isolation and R_{ik}, where $i \neq k$, is the added resistance when coils i and k are used in combination and therefore represents the correlated noise between coils.

An analogy can be made between the concept of the mutual noise resistance and that of a mutual inductance. Thus we find it useful to define an electric coupling coefficient, k_e, which is the electric analog of magnetic coupling defined in magnetically coupled circuits (15).

$$k_{e_{ik}} \equiv \frac{R_{ik}}{\sqrt{R_{ii} R_{kk}}}.$$ [10]

The electric coupling coefficient is used in later sections where we compare image reconstruction techniques. The electric coupling coefficient can also be thought of as a noise correlation coefficient.

Substituting [6] and [8] into [7] and squaring the result we obtain an expression for the SNR of a combination of coils.

$$\text{SNR}^2 = \frac{(\omega M V)^2}{4kT\Delta f} \frac{\sum_{i=1}^{N} \sum_{k=1}^{N} n_i n_k B_{ti} B_{tk} \cos(\phi_i - \theta_i - \phi_k + \theta_k)}{\sum_{i=1}^{N} \sum_{k=1}^{N} n_i n_k R_{ik} \cos(\phi_i - \phi_k)}.$$ [11]

To determine the relative gains and phase shifts that maximize the SNR we set $\partial(\text{SNR}^2)/\partial n_i$ and $\partial(\text{SNR}^2)/\partial\phi_i$ to zero for each value of i. The resultant set of equations are

$$B_{1i} \sum_{k=1}^{N} n_k B_{1k} \cos(\phi_i - \theta_i - \phi_k + \theta_k) = \text{SNR}^2 \sum_{k=1}^{N} n_k R_{ik} \cos(\phi_i - \phi_k) \qquad [12a]$$

$$B_{1i} \sum_{k=1}^{N} n_k B_{1k} \sin(\phi_i - \theta_i - \phi_k + \theta_k) = \text{SNR}^2 \sum_{k=1}^{N} n_k R_{ik} \sin(\phi_i - \phi_k). \qquad [12b]$$

where SNR^2 in the above expressions is given by [11]. To solve [12a] and [12b] for n_i and ϕ_i, the mathematics is made tractable by introducing complex notation with the following definitions.

$$b_i \equiv B_{1i} e^{j\theta_i} \qquad [13]$$

$$\alpha_i \equiv n_i e^{j\phi_i}. \qquad [14]$$

Substitution of [13] and [14] into [12a] and [12b] gives

$$\alpha_i^* e^{j\phi_i} \sum_{k=1}^{N} \alpha_k^* b_k + b_i e^{-j\phi_i} \sum_{k=1}^{N} \alpha_k b_k^* = \text{SNR}^2 (e^{j\phi_i} \sum_{k=1}^{N} \alpha_k^* R_{ik} + e^{-j\phi_i} \sum_{k=1}^{N} \alpha_k R_{ik}) \qquad [15a]$$

$$e^{j\phi_i} \sum_{k=1}^{N} \alpha_k^* b_k - b_i e^{-j\phi_i} \sum_{k=1}^{N} \alpha_k b_k^* = \text{SNR}^2 (e^{j\phi_i} \sum_{k=1}^{N} \alpha_k^* R_{ik} - e^{-j\phi_i} \sum_{k=1}^{N} \alpha_k R_{ik}). \qquad [15b]$$

where * denotes complex conjugate. Taking the sum and the difference of [15a] and [15b] and solving for b_i and b_i^* we obtain

$$b_i = \frac{\text{SNR}^2}{\sum_{k=1}^{N} \alpha_k b_k^*} \sum_{k=1}^{N} \alpha_k R_{ik} \qquad [16a]$$

$$b_i^* = \frac{\text{SNR}^2}{\sum_{k=1}^{N} \alpha_k^* b_k} \sum_{k=1}^{N} \alpha_k^* R_{ik}. \qquad [16b]$$

Equation [16a] is simply the complex conjugate of [16b] and thus only one is needed. In matrix form the set of equations corresponding to [16a] is

$$\mathbf{b} = \frac{\mathbf{R}\alpha}{\lambda}. \qquad [17]$$

where

$$\lambda \equiv \frac{\alpha^T \mathbf{b}^*}{\text{SNR}^2} \qquad [18]$$

and $\mathbf{b}$ and α are column vectors of the b_i's and α_i's and $\mathbf{R}$ is the square matrix of mutual noise resistances.

When solving [17] for α, λ can be treated as a constant. The absolute value of λ is only important for scaling the final image and does not affect the relative amplitudes

and phase shifts needed to combine the data from multiple coils. Holding λ constant, [17] corresponds to a set of linear simultaneous equations with the solution

$$\alpha = \lambda \mathbf{R}^{-1} \mathbf{b}, \tag{19}$$

where α is a complex column vector of relative amplitudes and phase shifts, $\mathbf{R}^{-1}$ is the inverse of the noise resistance matrix, and $\mathbf{b}$ is a complex column vector of the transverse fields created at point (x, y, z).

Equation [19] shows that the optimum weights and phase shifts are a function of position. Thus combining the data external to the computer with a single electronic circuit is only optimum at a single point. Each point or localized region needs a different combination of weights and phase shifts. Modifying the gains and phases corresponds to beam steering in phased array radar or ultrasound by phase shifting the time dependent signals. In radar and ultrasound the region of interest is generally at a distance large compared to the size of the receiving elements and wavelength in the array. Thus for a given point in the image, all of the elements receive a signal of approximately the same amplitude and amplitude corrections are unnecessary or small. For the NMR phased array both phase and amplitude corrections are important for determining the sensitive region. The NMR phased array operates in the near field and the coils which comprise the elements in the NMR phased array are comparable in size to the depth of the voxels of interest.

Each point in the image of the NMR phased array requires a different combination of time dependent signals and thus a different external circuit would be required for each region of the image. Since this is impractical, we attach a separate receiver chain to each of the coils, simultaneously collect the data from all coils and store the results. The data are combined later on a pixel by pixel basis with weights and phases that depend on location. In this way we obtain the highest possible SNR at all points in the image.

Because the process of Fourier transformation is linear, combining the quadrature time dependent signals with proper complex weighting is the same as combining the complex pixels after Fourier transformation. Transforming the data first and then combining complex pixels is more efficient because it requires only one complex Fourier transform for each coil. On the other hand, combining the time dependent signals first and then Fourier transforming would require a transform for each local region of the image. The number of transforms in this case might be as high as the number of pixels.

After Fourier transformation any algorithms that correct spatial distortions in the image due to nonlinear gradients (16, 17) can be applied. By Fourier transforming and remapping the data, the exact position of each pixel is known. Using either measured or calculated values for the RF field maps and noise resistance matrix, the separate complex images can then be phase shifted and added on a pixel by pixel basis according to [19] to arrive at a single composite image. If p_i is the resultant complex pixel value at point (x, y, z) due to coil i after Fourier transformation and remapping, the optimum combination of images yields the single pixel value P at point (x, y, z) given by

$$P = \lambda \mathbf{p}^{-1} \mathbf{R}^{-1} \mathbf{b}, \tag{20}$$

where $\mathbf{p}$ is the complex column vector of the p_i's.

)nce the data is combined into a single composite set of complex data, the final da t set can be treated as if it came from a single coil. If the end result is to form a m: :nitude image, the magnitude of the data set should be displayed. If the phase in' rmation is important, such as in spectroscopy, the data should be phased as if it ca ie from a single coil and displayed or further processed in the appropriate manner.

'ombined magnitude images. Here we determine the optimum way to combine m .gnitude images. Although this generally results in a slightly lower image SNR than m :ht be obtained for the more general case of combined complex images, combined m .gnitude images are simpler to implement. The phase shifts differences for each of th receiver channels do not have to be known and the commercial software for m nipulating, storing, and reconstructing magnitude images do not need to be modified to carry the complex data.

'ombined magnitude images are equivalent to choosing the external phase shifts in Fig. 7 to cancel the relative phase differences in the NMR signals due to the different di ection of the RF coils' magnetic fields. Thus the equation to maximize for SNR is [1] with $\phi_i = \theta_i$

$$\mathrm{SNR}^2 = \frac{(\omega M V)^2 \sum_{i=1}^{N} \sum_{k=1}^{N} n_i n_k B_{ti} B_{tk}}{4kT\Delta f \sum_{i=1}^{N} \sum_{j=1}^{N} n_i n_k R_{ik} \cos(\theta_i - \theta_k)}. \qquad [21]$$

1 king $\partial(\mathrm{SNR}^2)/\partial n_i$, assembling the equations, and solving for the n_i's yield the o timum weights n_i for combining magnitude images.

$$\mathbf{n} = \lambda \mathbf{r}^{-1} \mathbf{b}_t \qquad [22]$$

w iere $\mathbf{b}_t$ is a column vector of the B_{ti}'s, $\mathbf{n}$ is a column vector of the n_i's, and $\mathbf{r}$ is a n odified noise resistance matrix related to $\mathbf{R}$ by

$$r_{ik} = R_{ik} \cos(\theta_i - \theta_k). \qquad [23]$$

Sum-of-squares image. The image combination techniques above require detailed I nowledge of each coil's RF magnetic fields. However, in some cases the exact position (the coil may not be known, or perhaps the extra computation time associated with c alculating or measuring the RF magnetic fields is excessive. It is therefore highly (esirable to have a technique which combines the data without detailed knowledge (f the coils magnetic fields and at the same time preserves the high SNR of the phased array.

Since the NMR signal is proportional to the local RF field, the complex images are hemselves an estimate of the relative magnetic field strengths and directions. The higher the pixel SNR, the better the estimate. Since the images are only useful if the ixel SNR is higher than 20 (*14*) it seems reasonable to replace $\mathbf{b}$ in [20] by $\mathbf{p}^*$ (the onjugate of the pixel value is the appropriate quantity since increasing angles of the RF magnetic field correspond to time delays or a negative phase shift in the NMR signal). This, however, results in pixel intensities that are proportional to the square of the underlying NMR quantity to be measured. Thus after substitution we take the square root and obtain

$$P = \sqrt{\mathbf{p}' \mathbf{R}^{-1} \mathbf{p}^*}. \qquad [24]$$

In other words, each pixel value is the square root of the sum of the squares of the pixel values corresponding to the individual coils in the array. In this way we arrive at a method of combining images without computation or measurement of the magnetic fields.

To the extent that at least one coil in the array has a high pixel SNR and all coils have similar noise, combining the images as sum-of-squares results in a high SNR. A disadvantage, however, for a sum-of-squares image is related to artifact suppression. For example, suppose we have two coils, one placed on the abdomen and the other on the back. The image from the coil on the abdomen may have strong artifacts in the phase encoding direction due to motion. The image from the coil on the back would produce fewer artifacts. If these images are combined using knowledge of the magnetic fields, [20] tells us to weight the data from each coil by the RF field created by that coil. In regions where the RF field produced by the abdominal coil is low, the artifact is multiplied by a small number before its contribution is added to the composite image. If on the other hand the artifact is strong and the sum-of-squares method is used, the artifact is not suppressed because the pixel is weighted by itself and not a small field value. Figure 19 in the section on image results is an example of a sum-of-squares image showing a wrap around artifact in the phase encoding direction that does not appear in the corresponding image using field maps.

UNIFORM SENSITIVITY AND UNIFORM NOISE IMAGES

Although [20] shows how to optimally combine the signals from a multitude of coils and thus obtain the highest possible SNR at all points, it does not determine the choice of the overall scale factor, λ. Varying λ across an image can affect the appearance of the image in different ways. Two different distributions of λ are considered here, one corresponding to a uniform sensitivity image and the other corresponding to a uniform noise image.

Uniform sensitivity image. The data from each coil describes some common NMR quantity to be measured which ideally should be represented by the same pixel intensity or the same spectral amplitude, independent of the voxel location in space and independent of the RF coil sensitivity variation. Axel *et al.* (*18*) describes a method for correcting the intensity variation from a single coil. Here we derive a method for an array of receiving coils.

We know the NMR signal is proportional to the local magnetic field created by each coil. Specifically, the complex pixel value is proportional to the **b***. If data are combined in an optimal way by [20], λ must then be chosen such that the magnitude of P is independent of the relative amplitudes and directions of the RF magnetic fields of the coils. Thus we take expression [20], substitute **b*** for **p**, take the magnitude of the result, set it equal to a constant, and solve for λ. The result is

$$\lambda = \frac{C}{\sqrt{(\mathbf{b}^{*T}\mathbf{R}^{-1}\mathbf{b})(\mathbf{b}^{*T}\mathbf{R}^{-1}\mathbf{b})^*}},$$ [25]

where C is a constant that scales all pixels or spectra into a range suitable for display or storage in the computer.

since $\mathbf{R}^{-1}$ is a symmetric matrix, [25] reduces to

$$\lambda = \frac{C}{\mathbf{b}^T\mathbf{R}^{-1}\mathbf{b}^*} .$$ [26]

One can also show that λ in [26] is purely real although $\mathbf{b}$ is in general complex. Substitution of [26] into [20] yields the desired expression for combining the data of many coils into a single uniform sensitivity image that has optimized SNR at all points.

$$P = C\frac{\mathbf{p}^T\mathbf{R}^{-1}\mathbf{b}}{\mathbf{b}^T\mathbf{R}^{-1}\mathbf{b}^*} .$$ [27]

In a similar manner we can derive an expression for a uniform sensitivity image of combined magnitude data. The result is

$$P = C\frac{\mathbf{p}^T\mathbf{r}^{-1}\mathbf{b}_t}{\mathbf{b}_t^T\mathbf{r}^{-1}\mathbf{b}_t} .$$ [28]

where $\mathbf{p}$ and P are now pixel magnitudes as opposed to complex quantities.

Uniform noise image. An alternative choice of λ yields a uniform noise image. Such an image is a useful way to display the SNR variation of the composite image. Also, it is the phased array equivalent of a single surface coil image that has not had any intensity corrections applied.

From [8] the total noise power can be written in matrix form as proportional to R_{tot}.

$$R_{tot} = \alpha^T\mathbf{R}\alpha^*.$$ [29]

Substituting the optimum value of α given by [19] into [29] we obtain R_{tot} for optimally combined complex data.

$$R_{tot} = (\lambda\mathbf{R}^{-1}\mathbf{b})^T\mathbf{R}(\lambda\mathbf{R}^{-1}\mathbf{b})^* = \lambda^2\mathbf{b}^T\mathbf{R}^{-1}\mathbf{b}^*.$$ [30]

For a uniform noise image, λ in [30] is chosen so that R_{tot} is independent of the position. The functional form of λ must then be

$$\lambda = \frac{C}{\sqrt{\mathbf{b}^T\mathbf{R}^{-1}\mathbf{b}^*}} .$$ [31]

where C is an arbitrary constant that scales the image into a suitable range for display or storage. Substitution of [31] into [20] yields an expression for an optimized uniform noise image.

$$P = C\frac{\mathbf{p}^T\mathbf{R}^{-1}\mathbf{b}}{\sqrt{\mathbf{b}^T\mathbf{R}^{-1}\mathbf{b}^*}} .$$ [32]

In a similar manner we obtain a uniform noise image of combined magnitude data

$$P = C\frac{\mathbf{p}^T\mathbf{r}^{-1}\mathbf{b}_t}{\sqrt{\mathbf{b}_t^T\mathbf{r}^{-1}\mathbf{b}_t}} .$$ [33]

where $\mathbf{p}$ and P in [33] are pixel magnitudes as opposed to complex quantities.

QUANTITATIVE EVALUATION OF NOISE, INDUCTANCE, AND RECONSTRUCTION

Presented in the previous section is a range of possible methods for combining images. The highest possible SNR is expected in the composite image if noise correlations are taken into account. To better understand quantitatively the importance of the noise correlations we calculate the mutual inductance and mutual noise resistance matrix for the spine array of Fig. 3. The relative SNR obtained for the case of optimally combined complex images is then compared with optimally combined magnitude images and images in which the noise correlations are ignored altogether. Finally, using the calculated values for the noise resistance matrix the expected SNR improvement for a four element array is compared to the SNR obtained from a single large coil and a single small coil.

Mutual inductance and mutual noise resistance matrix. Here we calculate the mutual noise resistance and mutual inductance matrices between two coplanar coils as a function of the separation between the coil centers. As shown in Fig. 8. the RF coils are placed in a plane parallel to the surface of an infinite slab of a conducting material. The magnetic and electric fields in the slab and near the coil can be expressed in terms of a vector potential $\mathbf{A}$ (*19*).

$$\mathbf{B} = \nabla \times \mathbf{A} \qquad\qquad [34]$$

$$\mathbf{E} = -\frac{d\mathbf{A}}{dt} . \qquad\qquad [35]$$

We assume the low frequency limit whereby the local RF magnetic fields are primarily determined by currents in the RF coil and not significantly modified by the currents induced in the sample. In this case the vector potential can be expressed as an integral over the known current distribution in the coil. Further, we assume the
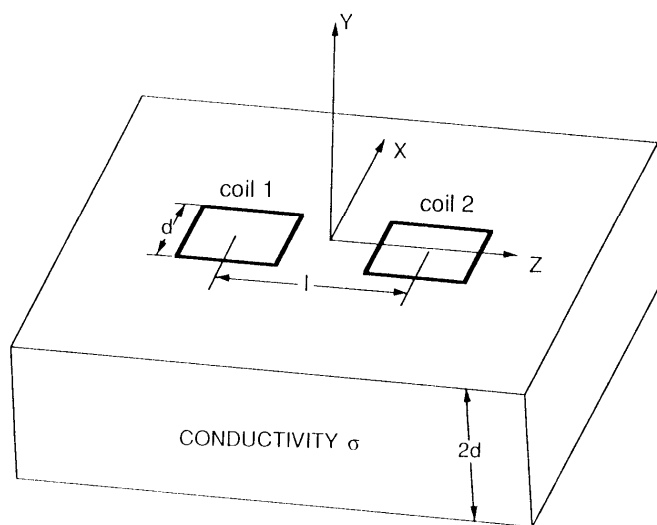

FIG. 8. Coil geometry for calculation of electric and magnetic coupling coefficients. Shown are square coils with dimension *d* placed above a slab of conducting material of thickness 2*d*.

cr ss-section of the conductors in the RF coil is small compared to the overall size of
the coil. The RF coil current can then be treated as a filament and the vector potential
can be written as a line integral over the current in the coil

$$A = \frac{\mu_0 I}{4\pi} \oint \frac{ds}{|r - r'|} .$$ [36]

where I is the current in the coil, s is a vector tangent to the conductor centerline with
a magnitude equal to the integrated distance along the centerline, and $r - r'$ is the
vector distance between a point on the conductor centerline and the observer.

Substitution of [36] into [34] yields the Biot–Savart Law (19) for the magnetic
field

$$B = \frac{\mu_0 I}{4\pi} \oint \frac{ds \times (r - r')}{|r - r'|^3} .$$ [37]

To estimate the mutual inductance, we use the fact that the line integral of the
vector potential around a closed loop is the flux linked through that loop. Thus the
mutual inductance between two filamentary coils can be expressed as the double integral

$$M_{ik} = \frac{\mu_0}{4\pi} \int \frac{ds_i \cdot ds_k}{|r_i - r_k|} .$$ [38]

where s_i is a vector tangent to the coil i's centerline and s_k is tangent to coil k's
centerline. The magnitude of s_i and s_k is the integrated distance along the centerline
of the coil and $r_i - r_k$ is the vector distance between a point on coil i and a point on
coil k.

To obtain an expression for the noise resistance in terms of the vector potential we
assume constant frequency and substitute [35] into [9].

$$R_{ik} = \omega^2 \sigma \int A_i \cdot A_k d^3 v.$$ [39]

Care must be taken to satisfy boundary conditions when applying [39] to other
geometries. In our case we have the two surfaces of the slab, each an infinite plane
parallel to the plane of the RF coil. Thus, according to [36], no electric fields are
perpendicular to the surface and [36] satisfies the boundary condition that the normal
component of the current density be zero. If the coil was rotated perpendicular to the
boundary, or the sample was truncated in the x or z dimensions, a scalar potential
could be introduced to match the boundary condition that the normal component of
current density be zero on the surface.

Figure 9 is a plot of the calculated electric and magnetic coupling coefficients between
two coplanar square coils as a function of the distance between the coil centers. The
curves were obtained by numerically integrating [38] and [39] and then normalizing
the results to values obtained at zero separation.

When calculating the vector potential, we avoid the singularity in [36] and [38]
by setting a minimum for $|r - r'|$. Physical considerations set this minimum distance
to be about equal to the radius of the wire. The results in Fig. 9 are for a wire size of
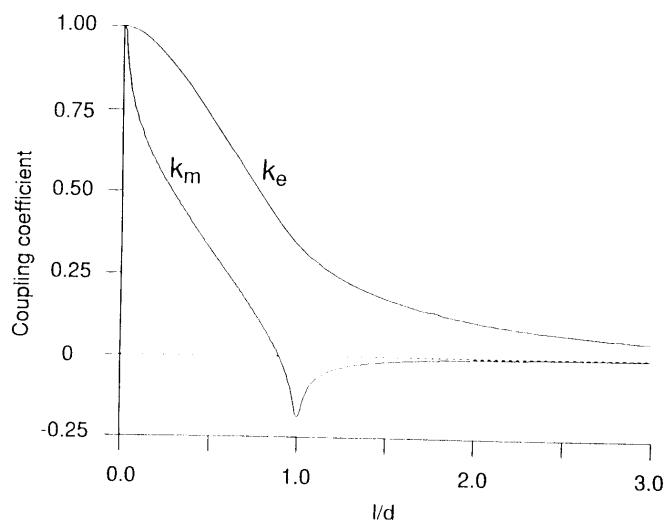$0.01d$, where d is the coil dimension. This corresponds to a wire radius of 1 mm for
a 10-cm coil.

FIG. 9. Plot of magnetic coupling coefficient and electric coupling coefficient as a function of the separation between two square coils (width d). The electric coupling coefficient, k_e was determined by numerically integrating [39] over a slab thickness of $2d$ with x and z limits of $\pm 10d$. The magnetic coupling coefficient, k_m, was determined by numerically integrating [38].

One intriguing aspect of these calculations is that they contradict assertions in the literature (20, 21) that coils with zero mutual inductance have no correlated noise. Figure 9 shows the coil overlap where the mutual inductance goes to zero (coil separation about $0.9d$), but the correlated noise (ke) does not. This is reasonable since the currents induced in the sample by the two coils share common paths. Thus a certain fraction of the random thermal motion of charges in the sample will produce correlated noise in the coils, even though there is no net flux linked between them. In the "Noise Measurements" section we describe experiments confirming this conclusion.

Using the curves in Fig. 9 we then construct magnetic and electric coupling matrices for the spine array of Fig. 3. The results are

$$
\mathbf{k}_m = \begin{bmatrix} 1 & 0 & 0.0078 & 0.0020 \\ 0 & 1 & 0 & 0.0078 \\ 0.0078 & 0 & 1 & 0 \\ 0.0020 & 0.0078 & 0 & 1 \end{bmatrix} \quad [40]
$$

$$
\mathbf{k}_e = \begin{bmatrix} 1 & 0.41 & 0.136 & 0.062 \\ 0.41 & 1 & 0.41 & 0.136 \\ 0.136 & 0.41 & 1 & 0.41 \\ 0.062 & 0.136 & 0.41 & 1 \end{bmatrix} . \quad [41]
$$

Comparison of reconstruction techniques. Although adjacent coils in Fig. 3 are positioned to have no mutual inductance, the electric coupling matrix given by [41] shows 41% correlated noise power. To understand the importance of noise correlations and their effect on images, we compare three methods of reconstruction: optimally

combining complex data; optimally combining magnitude data; and ignoring the noise correlations altogether.

To make the mathematics tractable we consider two surface coils. For optimally combined complex data, [19] is substituted into [11] to obtain the optimum SNR for two coils

$$\text{SNR}_{\text{opt}}^2 = \frac{(\omega M V')^2}{4kT\Delta f} \frac{\dfrac{B_{t1}^2}{R_{11}} + \dfrac{B_{t2}^2}{R_{22}} - \dfrac{2B_{t1}B_{t2}R_{12}}{R_{11}R_{22}}\cos(\theta_2 - \theta_1)}{1 - \dfrac{R_{12}^2}{R_{11}R_{22}}}.$$ [42]

The SNR for optimally combined magnitude images is found by taking [11] with $\phi_i = \theta_i$ and substituting [22] into the result for the n_i's.

$$\text{SNR}_{\text{mag}}^2 = \frac{(\omega M V')^2}{4kT\Delta f} \frac{\dfrac{B_{t1}^2}{R_{11}} + \dfrac{B_{t2}^2}{R_{22}} - \dfrac{2B_{t1}B_{t2}R_{12}}{R_{11}R_{22}}\cos(\theta_2 - \theta_1)}{1 - \dfrac{R_{12}^2}{R_{11}R_{22}}\cos^2(\theta_2 - \theta_1)}.$$ [43]

If the noise correlations are ignored altogether we take [19] with $R_{12} = 0$ and substitute the result into [11] to arrive at

$$\text{SNR}_{\text{nc}}^2 = \frac{(\omega M V')^2}{4kT\Delta f} \frac{\left(\dfrac{B_{t1}^2}{R_{11}} + \dfrac{B_{t2}^2}{R_{22}}\right)^2}{\left(\dfrac{B_{t1}^2}{R_{11}} + \dfrac{B_{t2}^2}{R_{22}}\right)^2 + \dfrac{2B_{t1}B_{t2}R_{12}}{R_{11}R_{22}}\cos(\theta_2 - \theta_1)}.$$ [44]

Equation [44] can also be obtained by taking [22] with $R_{12} = 0$ and substituting the results into [11]. This is because with noise correlations ignored, [19] tells us to combine the data in-phase, and combining the data in-phase is the same as combining magnitude images.

A measure of the SNR lost by combined magnitude images versus optimally combined complex data is given by the ratio of [43] to [42].

$$\left(\frac{\text{SNR}_{\text{mag}}}{\text{SNR}_{\text{opt}}}\right)^2 = \frac{1 - k_{c_{12}}^2}{1 - k_{c_{12}}^2\cos^2(\theta_2 - \theta_1)}.$$ [45]

The maximum for this expression is 1 when correlated noise power is 0 ($k_{c_{12}} = 0$) or when the signals are in phase ($\theta_2 - \theta_1 = 0$). The minimum occurs when the correlated noise is a maximum and the signals are $\pi/2$ out of phase ($\theta_2 - \theta_1 = \pi/2$). Numerical results given by [41] show that the maximum expected noise correlations are 41% ($k_{c_{12}} = 0.41$) when coils are overlapped. Substituting these values into [45] we obtain

$$0.91 \leq \frac{\text{SNR}_{\text{mag}}}{\text{SNR}_{\text{opt}}} \leq 1.$$ [46]

This shows that in the worst case less than 10% SNR is lost by combined magnitude images versus optimally combined complex data.

Since so little SNR is lost by combining magnitude images versus combining the complex data, it then seems reasonable to ask if the noise correlations can be totally ignored. The ratio of eqs. [44] to [42] is a measure of this loss and given by

$$\left(\frac{SNR_{nc}}{SNR_{opt}}\right)^2 = \frac{\left(\frac{B_{11}^2}{R_{11}} + \frac{B_{12}^2}{R_{22}}\right)^2 (1 - k_{c_{12}}^2)}{\left(\frac{B_{11}^2}{R_{11}} + \frac{B_{12}^2}{R_{22}}\right)^2 - \frac{4B_{11}^2 B_{12}^2 k_{c_{12}}^2}{R_{11} R_{22}} \cos^2(\theta_2 - \theta_1)}. \qquad [47]$$

The maximum of [47] is 1 when the correlated noise power is 0 ($k_{c_{12}} = 0$). The minimum occurs when the signals are out of phase ($\theta_2 - \theta_1 = \pi/2$) and the correlated noise is a maximum ($k_{c_{12}} = 0.41$). Equation [47] therefore has the bounds

$$0.91 \leq \frac{SNR_{nc}}{SNR_{opt}} \leq 1. \qquad [48]$$

It is interesting to note that these bounds are the same as those in [46]. This does not imply that optimally combined magnitude images are point by point identical in SNR to an image obtained by ignoring the noise correlations: it just means that both methods result in a similar maximum image degradation. We can see that it really does not matter which of the three ways the data is combined. All methods produce images with an SNR is that no more than 10% different from the others. Since ignoring noise correlations and combining magnitude images is the easiest to implement, it was the method of choice for our experiments described in the "Imaging" section.

Expected SNR improvements for a linear array. Using calculated noise resistances and RF magnetic fields, we wrote a computer program to estimate the SNR at the depth of the spine (~7 cm) for three different coil geometries: (1) a four element linear phased array made of 8-cm square coils, (2) a single large 15 × 30-cm rectangular coil, and (3) a single small 8-cm square coil.

The computer program was written for a phased array but also gives the correct answer for a single coil. The program first determines the noise resistance matrix by integrating [39] over the sample. Given a point in space, the magnetic field produced by each coil is numerically computed by integrating the Biot–Savart law (Eq. [37]) over a current filament placed at the centerline of the conductor. The resistance matrix and magnetic fields are then substituted into [19] to obtain the relative weight factors for combining signals from the coils. These weight factors along with the noise resistance matrix and magnetic fields are then substituted into [11] to obtain the SNR. Finally, the results are normalized to the ultimate sensitivity limit determined by Roemer and Edelstein (4). Figure 10 shows the results of our calculations.

Several aspects of these results are noteworthy. First, as expected, the ultimate sensitivity limit can be approached at a single point by imaging with a coil whose diameter is approximately equal to the depth of the voxel (3, 4). However, the four coil phased array achieves the SNR of a single small coil over the entire length of the array. On the other hand, a single rectangular coil with dimensions of 15 × 30 cm, a typical size for spine imaging, has a FOV comparable to the phased array but achieves only one-third of the SNR.
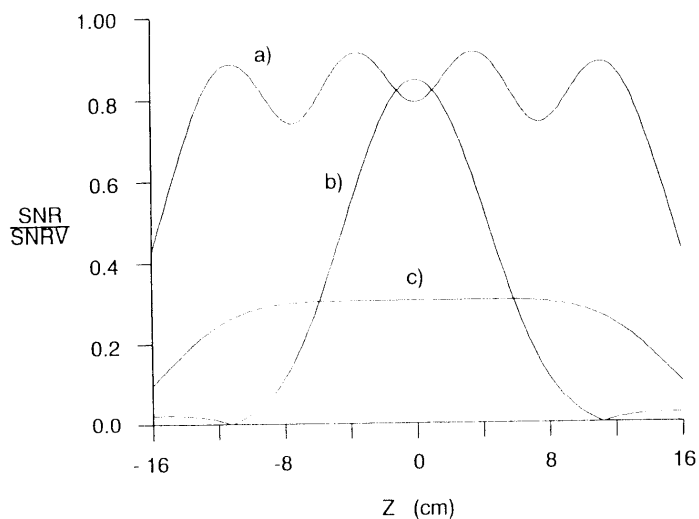
FIG. 10. Calculated SNR at a depth of 8 cm for three different surface coil arrangements: (a) a four element phased array made of 8-cm square coils; (b) a single 8-cm square coil; and (c) a single large 30 × 15-cm rectangular coil. An SNR of 1 corresponds to a theoretical upper limit SNRV given by Roemer and Edelstein (4) for linear reception.

NOISE MEASUREMENTS

The noise correlations between two overlapped coils were found in two ways: the noise resistances were determined directly with a vector impedance meter; and the correlations were measured with the NMR spectrometer.

Noise resistance measurements. Figure 11 shows the coil arrangement used to directly measure the noise resistance. Two coils are first independently tuned to the same frequency (~64 MHz). While measuring their magnetic response with a transmit and pickup loop and a spectrum analyzer, the coils are overlapped until the splitting of the resonances is reduced to a level below 10 KHz, forcing the mutual inductance of the coils to essentially zero. As indicated in Fig. 11, the coils are then cut at the
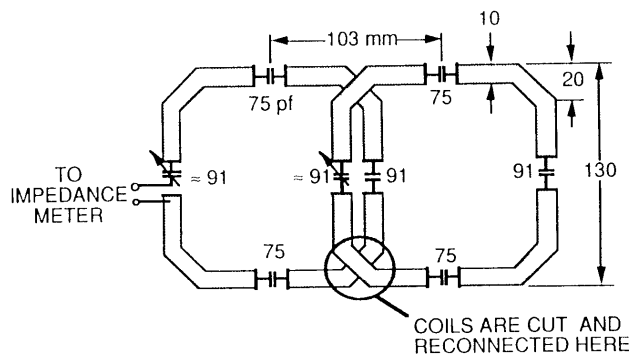

FIG. 11. Mutual noise resistance measurement. Coils are cut and reconnected series aiding or series opposing at the crossover point. The series impedance is measured on the edge of one of the coils as indicated.

crossover point and reconnected series aiding and series opposing. Table 2 shows the measured resistances of the series connected coils in air. on a salt water phantom, and on the back of a human subject.

The relatively large uncertainty for the measurements on the back is caused by repositioning errors that occur when the coil is removed, reconnected, and then returned to the back. For a phantom, the accuracy of returning the coil to its original position is good.

Table 2 shows that when the double coil is changed from series aiding to series opposing, we observe a small change of the resonant frequency, probably caused by repositioning errors of the connections when changed from series aiding to series opposing. A small change in frequency is consistent with a very small mutual inductance between the overlapped coils. On the other hand, with the coil placed on the sample we observe a large change in the noise resistances when the connection is changed.

From the resistance measurements in Table 2 we deduce the fractional noise correlations and compare the results with the calculated value of 41% given in [41]. Since the calculation involves sample losses we need only subtract from our measurement the uncorrelated noise due to random charge motion in the coils.

The resistance of two coils connected series aiding is given by

$$R_a = R_{ca} + R_{11} + R_{22} + 2R_{12}. \tag{49}$$

where R_{ca} is the resistance due to the dissipation in the coils. R_{11} and R_{22} are the sample losses for coil 1 and coil 2 in isolation, and R_{12} is the mutual noise resistance as defined by Eqs. [8] and [9]. For the series opposing connection the mutual noise resistance subtracts and we obtain

$$R_o = R_{co} + R_{11} + R_{22} - 2R_{12}. \tag{50}$$

Solving [49] and [50] for the fractional noise correlations we obtain a quantity numerically equal to the electric coupling coefficient

$$k_{e12} = \frac{R_{12}}{\sqrt{R_{11}R_{22}}} = \frac{R_a - R_o}{R_a + R_o - R_{ca} - R_{co}}. \tag{51}$$

TABLE 2

Measurement of Mutual Noise Resistance between Two Overlapped Coils

Sample	Connection	Resonant frequency (MHz)	Resistance (Ω)
None	Series aiding	64.44	0.56 ± 0.1
Phantom	Series aiding	63.63	12.95 ± 0.1
Back	Series aiding	63.90	20.0 ± 0.5
None	Series opposing	63.93	0.60 ± 0.1
Phantom	Series opposing	63.32	6.31 ± 0.1
Back	Series opposing	63.30	12.6 ± 0.5

Note. The phantom contains a 0.04 M NaCl solution and is rectangular with dimensions 48 × 24 × 30 cm. The overlapped coils were placed in the center of the largest face of the phantom with the long axis in the direction of coil overlap.

where we have assumed that $R_{11} = R_{22}$. Substituting the measured values from Table 2 into [51], we obtain the noise correlations for the phantom and patient:

$$k_{e_{12}} = \begin{cases} 0.356 \pm 0.008, & \text{phantom} \\ 0.231 \pm 0.023, & \text{back.} \end{cases} \qquad [52]$$

If we compare the measured results in [52] with the calculated value of 41% we find that the measured values are somewhat low. However, this difference is not unreasonable since the calculation ignores penetration artifacts (22) and does not take into account the sample boundaries which distort the induced currents in the x and z dimensions.

A general trend is that the noise correlations follow the size of the sample. The calculation for coils against an infinite slab shows the greatest correlation, the measured noise on the phantom the next largest, and the noise measured on the back the smallest. This can be explained on physical grounds by considering the nature of the field solutions. The currents induced in the sample at points far from the coils have common shapes and paths. Much of the noise correlations can be expected to come from these currents because correlated noise arises from common currents. Thus if we reduce the size of the sample, we can expect to reduce the correlated noise.

Perhaps the most important lesson of these measurements is to show that sample geometry has a significant effect on the amount of correlated noise. Therefore one should use noise correlations measured on a patient by patient basis rather than calculated or previously measured values. Measurement of the noise can be done at the beginning or end of a scan by sampling each of the channels with the RF transmitter off. Such noise measurements have the additional advantage that they include the uncorrelated components of noise from the preamplifier and coil.

Noise correlation measurements using the NMR spectrometer. To confirm that measurement of the mutual noise resistance is equivalent to a direct measurement of the correlated noise, we connected each of the overlapped coils to its own preamplifier and measured the noise correlations at the output of the preamplifiers using a signal combiner and NMR receiver. Figure 12 shows the experimental arrangement.
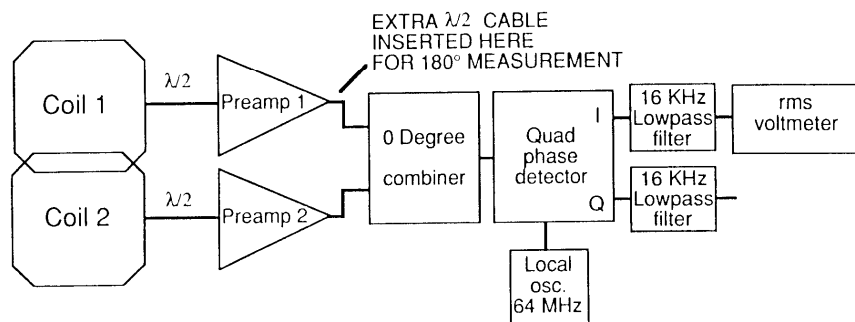

FIG. 12. Correlated noise measurement. RMS voltage measurements are first made with identical cables between the preamplifiers and zero degree combiner. An extra half-wave cable is placed between preamplifier 1 and the combiner for noise measurement of coil outputs 180° out of phase. The local oscillator is set to 63.886 MHz and the low pass filter bandwidth is 16 kHz.

The signals at the output of the preamplifiers are added or subtracted by connecting the outputs to a zero degree combiner with different length cables. The signals are added in-phase by attaching identical length cables between the preamplifiers and the combiner. The signals are added 180° out of phase by placing an extra $\lambda/2$ cable between one of the preamplifiers and the combiner. The output of the combiner is connected to the NMR receiver and the rms noise is measured at baseband.

The difference between the noise power for outputs added in-phase and outputs added out of phase is twice the correlated noise power, and the sum is twice the uncorrelated noise. The fractional noise correlations at the output of the preamplifiers is therefore

$$\frac{\langle v_{n1} v_{n2} \rangle}{\langle v_{n1}^2 \rangle} = \frac{v_0^2 - v_{180}^2}{(v_0^2 + v_{180}^2)} . \qquad [53]$$

where v_0 is the rms voltage measured when the preamplifier outputs are added in-phase, v_{180} is the rms noise when the preamplifiers outputs are added 180° out of phase, and $\langle \ \rangle$ denotes time average. Equation [53] assumes that the noise power at the output of preamplifiers is identical ($\langle v_{n1} \rangle = \langle v_{n2} \rangle$). This condition was forced on the coils and the preamplifiers by careful construction and subsequent adjustment.

Before we can compare with our previous measurement, we need to modify [53] by subtracting out the thermal noise in the coil and the electronics. The fractional increase in uncorrelated noise power due to thermal noise in the coil is given by

$$\left(\frac{1}{1 - (R_L / R_1)} \right), \qquad [54]$$

where R_L and R_1 are the loaded and unloaded resistance as measured at the terminals of the coils (including cable). The fractional increase in uncorrelated noise power due to the electronics is given by

$$\left(\frac{1 - (T_{cold} / T_{warm})}{1 - (v_{cold}^2 / v_{warm}^2)} \right), \qquad [55]$$

where v_{warm} is the rms noise voltage measured with room temperature 50 Ω resistors attached to the inputs of the preamplifiers and v_{cold} is the rms noise voltage measured with the resistors placed in liquid nitrogen.

Because the coil and preamplifier noises are uncorrelated, they only contribute to the denominator of [53]. Thus we multiply [53] by [54] and [55] and obtain an expression for the fractional noise correlations due to sample noise only, a quantity that is numerically equal to the electric coupling coefficient.

$$k_{e_{12}} = \frac{\langle v_{n1} v_{n2} \rangle}{\langle v_{n1}^2 \rangle} = \frac{(v_0^2 - v_{180}^2)}{(v_0^2 + v_{180}^2)} \frac{1}{(1 - R_L / R_E)} \left(\frac{1 - (T_{cold} / T_{warm})}{1 - (v_{cold}^2 / v_{warm}^2)} \right). \qquad [56]$$

Table 3 summarizes the measurement results for the coils placed on a rectangular salt water phantom. There is good agreement between these results and [52] where k_{12}^c was determined by directly measuring the noise resistances on the same phantom. Thus we confirm that noise correlations can exist even when the mutual inductance between two coils is zero and demonstrate that claims to the contrary (20, 21) are incorrect.

TABLE 3

Noise Correlation Measurements between Two Overlapped Coils

v_0 (mv)	v_{180} (mv)	v_{cold} (mv)	v_{warm} (mv)	T_{cold} (K)	T_{warm} (K)	R_L (Ω)	R_E (Ω)	$k_{e_{12}}$
112 ± 1	88 ± 1	59 ± 1	101 ± 1	77	294	50	494	0.349 ± 0.017

IMAGING

Apparatus. To test our reconstruction ideas with imaging we built two linear four element spine imaging arrays, one consisting of 12-cm coils and the second made with 8-cm coils. Figure 13 is a photograph and Fig. 14 is a schematic of the larger array.

A number of the array details are worthy of comment. First, a passive blocking circuit employing crossed diodes (*23*) is placed on the side of each coil to eliminate induced RF currents during transmit. Second, to minimize noise coupling during receive, [2] tells us to place an inductor at the output of each coil tuned to resonate with the output capacitor. Rather than place an inductor at the coil output, we tune the capacitor in the input stage of the preamp (Fig. 6) to yield the correct inductance as viewed from the preamp input terminals.
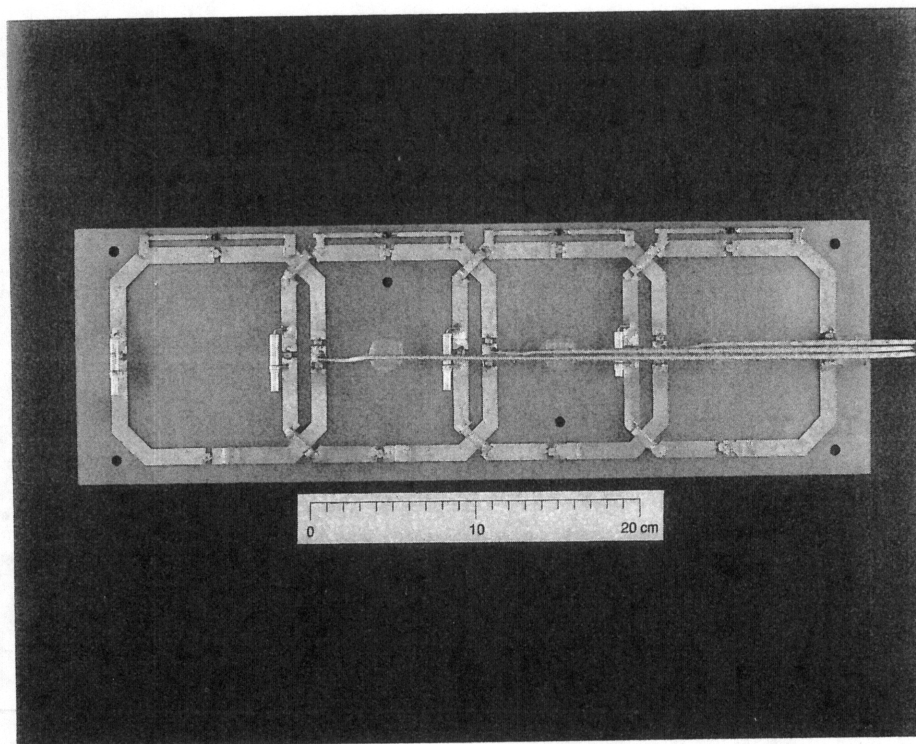

FIG. 13. Photograph of four element spine array for imaging a 48-cm FOV. Passive blocking circuits are made on the sides of the array. The cables are routed through the center of the array to eliminate the need for baluns.
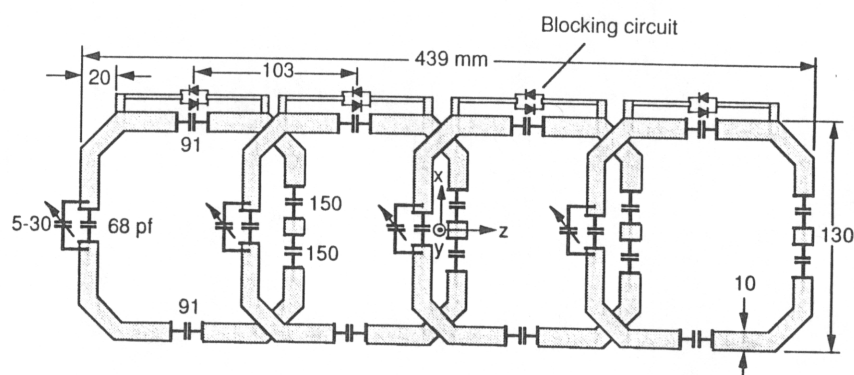
FIG. 14. Schematic diagram of coil in Fig. 13 showing component values and dimensions.

Another important point is the location of the output cables. To eliminate baluns the cables are routed and connected in the middle of the array rather than on the sides. This choice of cable position can be understood by examining the electric fields. By symmetry none of the coils excite an electric field parallel to the $x = 0$ plane, and thus this plane is ideally at a constant electric potential. Therefore placing the cables in the $x = 0$ plane has little effect on the electric fields. The electric fields on the sides of the array are complicated and vary from point to point so placement of cables without baluns at these points would short out electric fields and create circulating currents which ultimately show up as a change in impedance and increased losses as seen from the coil terminals.

The four channel receiver system shown in Fig. 15 was constructed to acquire the data. The NMR signals simultaneously pass through four identical receiver channels. Each channel has its own A/D converter and digital storage buffer. The buffer for each channel is only large enough to store the data for a single excitation and thus the data must be transferred to the computer between successive excitations. This is done during a time that is normally used for acquiring other slices or echoes. Thus for our experiment we sacrificed the ability to acquire multiple slices and multiple echoes. Future hardware will not have this limitation.

The preamplifier gain and receiver gain in each channel was adjusted to be identical. This results in NMR signals at the output of the receivers that all have the same amplification, even under loaded conditions. NMR signal gains that are independent of sample loading is another advantage of connecting low input impedance preamplifiers to the coils. To understand this effect, consider the preamplifier and attached coil of Fig. 5. By design the preamplifier plus inductor is chosen to resonate with the output capacitor C_{2b} and to present a high impedance in series with the coil. Hence the NMR voltage across C_{2b} is independent of the series resistance R_1 (R_1 is the combined coil and sample losses). In effect a low input impedance preamplifier attached to a coil measures the open circuit voltage of the coil. Use of low input impedance preamplifiers on receive is therefore analogous to transmitting with a low output impedance power amplifier to force a constant voltage and thus produce a constant NMR flip angle independent of sample loading (24).
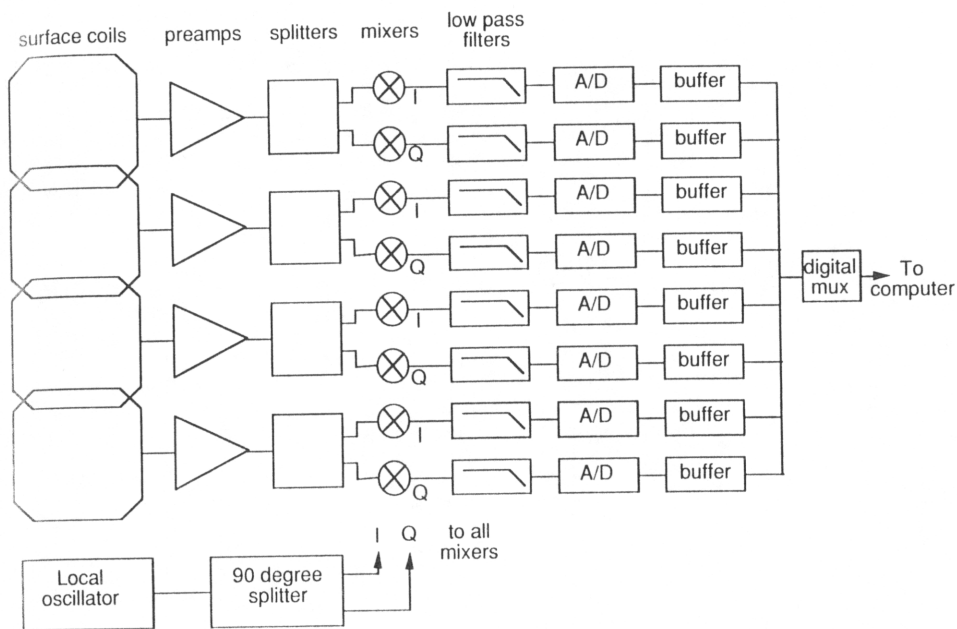
FIG. 15. NMR phased array system architecture. Each coil has its own NMR receiver chain and 1024 deep digital storage buffer. All receivers operate from the same local oscillator frequency and the data on all channels are sampled at the same time.

FIG. 16. Four sagittal images taken with the spine array shown in Fig. 13. Although all four coils are simultaneously receiving data, there is no sign of coupling between coils. FOV = 48 cm, 512 × 512 pixels, NEX = 2, 5 mm slice, T_R = 400 ms, T_E = 20 ms, imaging time = 6:50, B = 1.5 T. Phase encoding is in the y direction. Only the central 256 points in the horizontal direction are shown. Artifacts at the top and bottom of the images are due to wraparound.

Imaging results. Figure 16–22 show typical imaging results in the area of the lumbar and thoracic spine. Figure 16 shows images reconstructed from the data acquired by the individual coils in our four-element phased array. Note that although all four coils are simultaneously active and receiving NMR signals, each image shows virtually no coupling to other coils. If any significant signal was coupled to a given coil from another, a partial image from the second coil would be superimposed on the first coil's image. As further evidence, each image contains only two nulls with each null corresponding to the location of a single conductor crossing the sagittal plane. If significant signal was coupled between coils we would expect multiple nulls or at least significant variation in the intensity corresponding to the conductor locations of the other coils. Since the images show no significant NMR signal transferred between coils, we also know that no significant noise is transferred and hence each coil is independently receiving from its own region. The artifacts at the top or bottom of the images are not related to coupling. These are wraparound artifacts which are automatically suppressed in some of the composite images.

Figure 17 is a uniform noise image obtained by combining the four separate images according to [33] with $R_{ii} = 1$ and $R_{ik} = 0$, where $i \neq k$. Figure 18 is a uniform sensitivity image obtained using [28] with $R_{ii} = 1$ and $R_{ik} = 0$.

In constructing composite images, we ignored the correlated noise because our analysis above indicates that the impact on the image will be small. Also, each coil in the spine array loaded a similar amount and thus the noise resistances of the coils were assumed to be identical. In general this is not the case and in the future we intend to automatically measure the noise resistance by sampling the digitizer with the RF
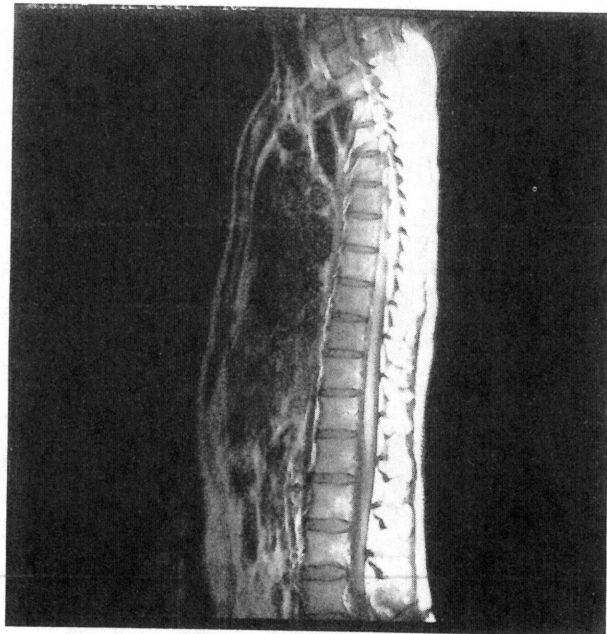

FIG. 17. Uniform noise image. The data of Fig. 16 were combined using Eq. [33] with noise correlations ignored ($R_{ik} = 0$, where $i \neq k$).

transmitter off. This allows us to determine the noise resistance matrix on a patient by patient basis, including noise correlations.

In Fig. 18 there is a variation of intensity on the anterior surface of the patient and a more pronounced circular variation at the ends of the array, again inside the patient. These variations are created by errors in the field calculation. Expressions for the magnetic fields are obtained by integrating the Biot–Savart Law (Eq. [37] with $|\mathbf{r} - \mathbf{r}'| \geqslant 5$ mm) over a filament of current placed at the centerline of each coil. Since this approximation is good for distances large compared to the wire size we observe intensity variations in the portion of the image near the coils. The circular variations at the ends of the array are more pronounced because there is no overlapping coil to provide information in that region. In the region of the spine, however, the filamentary approximation is very good and the image is highly uniform.

Figure 19 is a sum-of-squares image. Note that the pronounced wraparound artifacts at the top and bottom are not present to any significant degree in the uniform noise image (Fig. 17); otherwise, both images are essentially identical. This is a good example of poor artifact rejection of a sum-of-squares image, for reasons discussed earlier.

Hybrid images for improved display. Both the uniform noise image and the uniform sensitivity images have aspects that are aesthetically displeasing. It is difficult to display or photograph the uniform noise image in a satisfactory way because of dynamic range limitations of the eye, monitor, and film. On the other hand, the uniform sensitivity image can emphasize noise in regions of the image that are not of use or interest,
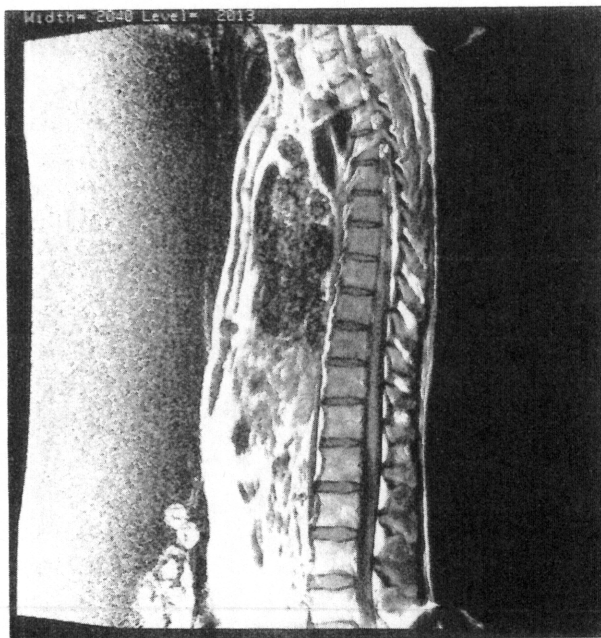

FIG. 18. Uniform sensitivity image. The data of Fig. 16 were combined using Eq. [28] with noise correlations ignored ($R_{ik} = 0$, where $i \neq k$). Note that on the anterior side of the patient near the edge of the image the noise is amplified excessively.
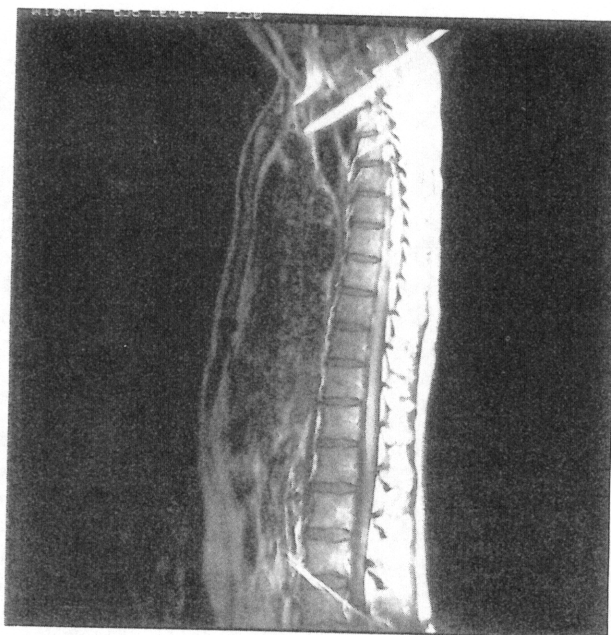
FIG. 19. Sum-of-squares image. The data of Fig. 16 were combined using Eq. [24] with noise correlations ignored ($R_{ik} = 0$, where $i \neq k$). Note the artifacts at the top and bottom of the image which appear as a bright diagonal line. Except for this poorer artifact suppression this image is virtually identical to the uniform noise image (Fig. 17).

especially near the edge of the image farthest from the array. We therefore find it useful to use a hybrid approach that automatically produces a uniform sensitivity image in regions with high SNR and a uniform noise image in the regions with low SNR.

Equation [27] shows how to construct a uniform sensitivity image and [32] shows how to produce a uniform noise image. The only difference between the two methods is an extra factor of $\sqrt{\mathbf{b}^T \mathbf{R}^{-1} \mathbf{b}^*}$ in the denominator of [27] which is only a function of the coils' magnetic fields and the noise resistances. For purposes here we assign it the variable $\Psi = \sqrt{\mathbf{b}^T \mathbf{R}^{-1} \mathbf{b}^*}$. Physically, Ψ is a measure of the SNR as a function of position, with larger values corresponding to points of higher SNR.

To construct a hybrid image we first determine Ψ_{max}, the maximum value of Ψ, from calculated or measured RF field maps and noise resistances. The point in space associated with this maximum is found near the RF coils because the maximum occurs where the RF field is largest. At some distance from the coils the SNR is reduced to a level such that noise dominates over the image data. We therefore assign a threshold value of SNR, $\epsilon\Psi_{max}$ where ϵ is a small number. For points with $\Psi > \epsilon\Psi_{max}$, the data is combined as a uniform sensitivity image and for points with $\Psi \leqslant \epsilon\Psi_{max}$, the data is combined as a uniform noise image. We have found that the exact choice of ϵ is not particularly important; ϵ can vary by a factor 5 or more and still produce a uniform sensitivity region of the image and not magnify the noise level in other

parts too much. This is because the useful portion of the image should have pixel SNRs that are at least 20 (*14*).

To obtain a smooth transition between the uniform noise and uniform sensitivity parts of the image, the solutions are matched in a continuous manner. From [27] and [32] a hybrid image with this property is given by

$$
P = C\mathbf{p}^{T}\mathbf{R}^{-1}\mathbf{b}
\begin{cases}
\dfrac{1}{\psi^{2}}, & \text{if} \quad \psi \geq \epsilon\psi_{max} \\[2mm]
\dfrac{1}{\psi\epsilon\psi_{max}}, & \text{if} \quad \psi < \epsilon\psi_{max},
\end{cases}
\tag{57}
$$

where

$$
\psi = \sqrt{\mathbf{b}^{T}\mathbf{R}^{-1}\mathbf{b}^{*}} .
\tag{58}
$$

Figure 20 shows a hybrid image constructed with $\epsilon = 0.02$. The image has the best overall properties of the uniform noise and uniform sensitivity image and results in an outstanding 512×512 spin-echo image of the thoracic and lumbar spine acquired in less than 7 min. Figure 21 is a $2\times$ magnification of the central portion of the image showing detail.

Figure 22 shows results taken with a second four element spine array. The elements in this array were chosen to be 8 cm versus 12, a better match to the depth of the
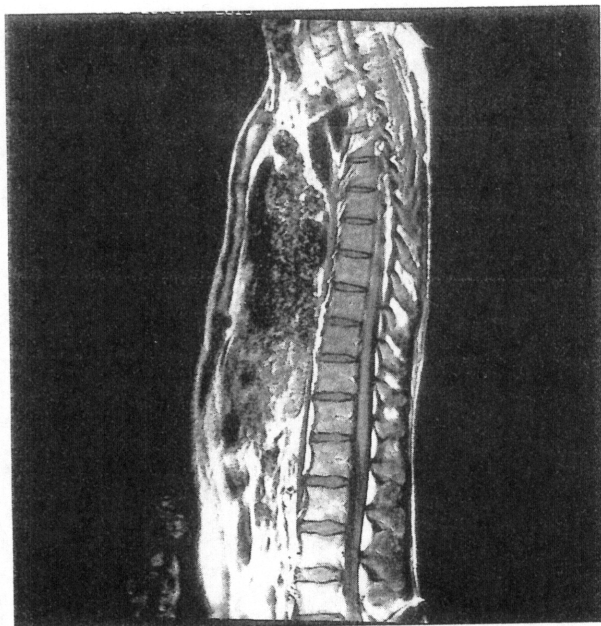

FIG. 20. Hybrid image. The data of Fig. 16 were combined using Eq. [57] with $\epsilon = 0.02$. In the regions of high SNR, such as the spinal area, the image is a uniform noise image. In regions of low SNR, such as the anterior side of the body the display is a uniform noise image.

FIG. 21. 2× magnification of central portion of Fig. 20 showing detail. The image is equivalent to a 256 × 256 image with a 24-cm FOV.

spine (∼7 cm). This resulted in 1.5 times greater SNR and allowed an increase in resolution. The pixel size in Fig. 22 is $0.625 \times 0.625 \times 5$ mm and the imaging time was under 7 min. Since our hardware limits us to four coils, we reduce the FOV to 32 cm.

The SNR obtained with the two spine arrays was compared to the SNR obtained with a single 15×30 cm rectangular coil. At the depth of the vertebral body (∼7 cm), the four element spine array showed ∼2 times higher SNR than the rectangular coil and the spine array made with 8-cm surface coils achieved ∼3 times the SNR of the rectangular coil. These measurements are in reasonable agreement with our calculated values in Fig. 10.

Making arrays with coils smaller than 8 cm are not expected to yield significant further improvements in SNR at the spine. This is because a coil with a diameter d, where d is the depth of interest, achieves 90% of the ultimate SNR limit (3, 4). We do, however, expect a 20% further improvement in SNR by the addition of coils to both sides of the linear array due to "quadrature effects" (4).

SUMMARY AND CONCLUSIONS

The results presented here show the first practical applications of truly simultaneous imaging from an NMR phased array of closely positioned surface coils. By this means we obtain the high SNR of a small surface coil over fields-of-view usually associated with volume coils, with no increase in imaging time.
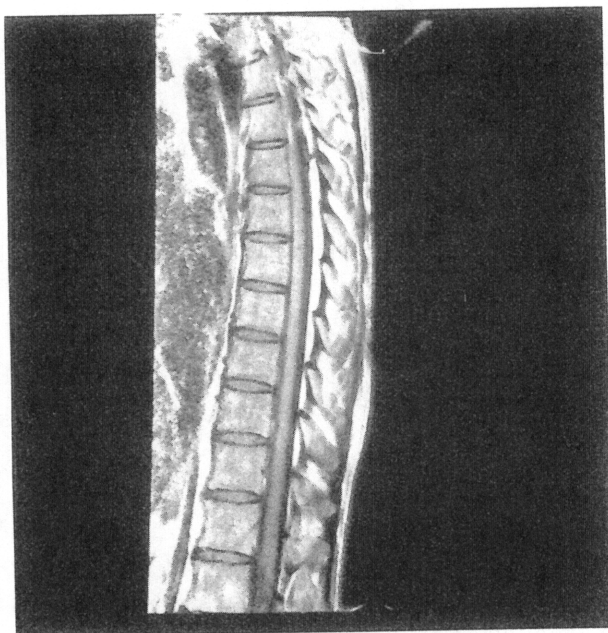
FIG. 22. Uniform sensitivity image taken with the smaller four element spine array. The coils are 8 cm wide. FOV = 32 cm, 512 × 512 pixels, NEX = 2, 5 mm slice, T_R = 400 ms, T_E = 25 ms, imaging time = 6:50. The central 256 pixels in the horizontal direction are shown.

In order to accomplish this task we have eliminated interactions among coils by overlapping adjacent coils and connecting all coils to low input impedance preamplifiers. Overlapping adjacent coils forces the mutual inductance between neighboring coils to zero. By attaching all coils to low input impedance preamplifiers, we reduce the current amplitude flowing in the coils during reception and essentially eliminate the interaction with next nearest neighbor and farther coils.

To obtain the highest possible SNR at all points in the image, the data from each of the coils must be separately received, stored, and then combined with weights that depend on the location of the voxel. This has a profound impact on the system complexity and software because the hardware and data handling requirements scale with the number of coils.

A variety of mathematical algorithms were derived that determine weights for combining both image and spectroscopic data. For high SNR, the most desirable method [20] is the most complicated because it requires detailed RF field maps, correlated noise measurements, and the manipulating of complex data. An algorithm which combines magnitude images [22] does not require manipulation of complex image data or knowledge of receiver phase shifts. A sum-of-squares method [24] has the advantage that it does not use the coils' positions or RF field maps. The simpler methods lose only about 10% of the maximum possible SNR. The sum-of-squares method has the additional disadvantage that it does not suppress artifacts as well as the other techniques that use RF field maps.

We derived uniform noise and uniform sensitivity methods for display of optimally combined complex images (Eqs. [27] and [32]) and optimally combined magnitude images (Eqs. [28] and [33]). Both approaches have identical SNRs but appear different because of dynamic range limitations of the eye, monitor, and film. A hybrid approach given by Eq. [57] combines the best overall properties of uniform noise and uniform sensitivity images. It yields a uniform sensitivity image in regions of high SNR and limits the noise in low SNR regions.

Spin-echo images from two four element spine arrays were acquired and various image combination techniques were applied to the data. For imaging the spine, measurements of SNR using the phased array showed increases of 2 to 3 over that obtained with a typical rectangular coil (30 × 15 cm) and FOVs of 48 and 32 cm, values normally associated with volume body images.

The techniques described here are generic and apply to all forms of imaging and spectroscopy where a large FOV is desired. We hope in the future to apply these ideas to arrays of 16, 32, or even more coils. The improvements in SNR are substantial and in the long term we believe that virtually all clinical imaging systems will use phased arrays for most imaging and spectroscopy procedures. The development will be challenging since the resulting large amount of data will require a large increase in associated hardware and software.

REFERENCES

1. P. B. ROEMER, W. A. EDELSTEIN, S. P. SOUZA, C. E. HAYES, AND O. M. MUELLER, "SMRM 7th Annual Meeting," p. 875, 1988.
2. P. B. ROEMER, W. A. EDELSTEIN, S. P. SOUZA, C. E. HAYES, O. M. MUELLER, AND R. L. HARRIS, "RSNA 74th Annual Meeting," paper 1239, p. 378, 1988.
3. W. A. EDELSTEIN, T. H. FOSTER, AND J. H. SCHENCK, "SMRM 4th Annual Meeting," p. 964, 1985.
4. P. B. ROEMER AND W. A. EDELSTEIN, "SMRM 6th Annual Meeting," p. 410, 1987.
5. J. F. SCHENCK, H. R. HART, T. H. FOSTER, W. A. EDELSTEIN, AND M. A. HUSSAIN, in "Magnetic Resonance Annual, 1986" (H. Kressel, Ed.), pp. 123–160, Raven Press, NY, 1986.
6. S. BEER, "NMR Antenna and Method for Designing the Same," U.S. Patent 4682112, July 21, 1987.
7. J. S. HYDE, A. JESMANOWICZ, W. FRONCISZ, J. B. KNEELAND, AND T. M. GRIST, J. Magn. Reson. 70, 512 (1986).
8. C. J. HARDY, R. W. KATZBERG, R. L. FREY, J. SZUMOWSKI, S. TOTTERMAN, AND O. M. MUELLER, Radiology 167, 835 (1988).
9. S. M. WRIGHT, R. L. MAGIN, AND J. R. KELTON, "SMRM 6th Annual Meeting," p. 96, 1987.
10. E. B. BOSKAMP, "SMRM 6th Annual Meeting," p. 405, 1987.
11. R. TYRRELL AND H. REQUARDT, "SMRM 6th Annual Meeting," p. 408, 1987.
12. O. M. MUELLER AND W. A. EDELSTEIN, "SMRM 6th Annual Meeting," p. 411, 1987.
13. D. I. HOULT AND R. E. RICHARDS, J. Magn. Reson. 24, 71 (1976).
14. W. A. EDELSTEIN, G. H. GLOVER, C. J. HARDY, AND R. W. REDINGTON, Magn. Reson. Med. 3, 604 (1986).

15. Staff of the Department of Electrical Engineering at MIT, "Magnetic Circuits and Transformers," MIT Press, Cambridge, MA, 1946.

16. I. SEKIHARA, M. KUIDA, AND H. KOHNO, *Phys. Med. Biol.* **29,** No. 1, 15 (1984).

17. A. PARKER, R. V. KENYON, AND D. E. TROXEL, *IEEE Trans. Med. Imaging* **MI-2,**(1) (1983).

18. L. AXEL, J. CONSTANTINI, AND J. LISTERUD, *Amer. J. Roentgenol.* **148,** 418 (1987).

19. W. R. SMYTHE, "Static and Dynamic Electricity," 3rd ed., McGraw–Hill, New York, 1968.

20. A. JESMANOWICZ AND J. S. HYDE, "SMRM 6th Annual Meeting," p. 412, 1987.

21. J. S. HYDE, A. JESMANOWICZ, AND J. KNEELAND, "RSNA 74th Annual Meeting," paper 218, p. 86, 1988.

22. G. H. GLOVER, C. E. HAYES, N. J. PELC, W. A. EDELSTEIN, O. M. MUELLER, H. R. HART, C. J. HARDY, M. ODONNELL, AND W. D. BARBER, *J. Magn. Reson.* **64,** 255 (1985).

23. W. A. EDELSTEIN, C. J. HARDY, AND O. M. MUELLER, *J. Magn. Reson.* **67,** 156 (1986).

24. W. A. EDELSTEIN, O. M. MUELLER, R. L. FREY, AND D. M. VATIS, "SMRM 6th Annual Meeting," p. 372, 1987.